Journal of ELECTRONIC MATERIALS, Vol. 46, No. 10, 2017
DOI: 10.1007/s11664-017-5616-4

Magnetic, Electric and Optical Properties of Mg-Substituted Ni-Cu-Zn Ferrites

S.M. KABBUR,[1] U.R. GHODAKE,[1] RAHUL C. KAMBALE,[2] S.D. SARTALE,[2] L.P. CHIKHALE,[3] and S.S. SURYAVANSHI[3,4]

1.—Department of Physics and Electronics, Shri Shivaji Mahavidyalaya, Barshi, Maharashtra 413411, India. 2.—Department of Physics, Savitribai Phule Pune University, Ganeshkhind, Pune, Maharashtra 411007, India. 3.—School of Physical Sciences, Solapur University, Kegaon, Solapur, Maharashtra 413255, India. 4.—e-mail: sssuryavanshi@rediffmail.com

The $Ni_{0.25-x}Mg_xCu_{0.30}Zn_{0.45}Fe_2O_4$ (x = 0.00 mol, 0.05 mol, 0.10 mol, 0.15 mol, 0.20 mol and 0.25 mol) magnetic oxide system was prepared by a sol–gel auto–combustion method using glycine as a fuel. X-ray diffraction study reveals the formation of pure spinel lattice symmetry along with the presence of a small fraction of unreacted Fe_2O_3 phase as a secondary phase due to incomplete combustion reaction between fuel and oxidizer. The lattice constant (a) was found to decrease with the increase of Mg^{2+} content; the average crystallite size (D) is observed in the range of 26.78–33.14 nm. At room temperature, all the samples show typical magnetic hysteresis loops with the decrease of magnetic moment (n_B) of Ni-Cu-Zn ferrites with the increase of Mg^{2+} content. The intrinsic vibrational absorption bands for the tetrahedral and octahedral sites of the spinel structure were confirmed by infrared (IR) spectroscopy. The optical parameters such as refractive index (η), velocity of IR waves (v) and jump rates (J_1, J_2, J) were studied and found to be dependent on the variation of the lattice constant. The Curie temperature (T_c) of Ni-Cu-Zn mixed ferrite was found to decrease with Mg^{2+} addition. The composition x = 0.15 mol.% with a low dielectric loss tangent of 2% seems to have potential for multilayer chip inductor applications at a wide range of frequencies.

Key words: Ferrites, x-ray diffraction, IR spectroscopy, optical parameters, dielectric properties

INTRODUCTION

Ni-Cu-Zn ferrites are soft magnetic materials useful in the radio frequency (RF) region and are mainly utilized for multilayer chip inductor (MLCI) devices due to their relatively good structural, optical, magnetic, electrical and dielectric properties at high frequencies.[1–3] MLCI is used in promising electronic applications like notebook computers, video cameras and cellular phones.[4] The important requisites of MLCI are the good quality factor, high electrical resistivity, high permeability and low eddy current loss. These properties are useful for the reduction in the number of layers to minimize the capacity between the layers, hence leading to miniaturization of the electronic components.[5–7] Mg-based ferrites are used in microwave devices because they have high electrical resistivity (10^9 Ω-cm) and low dielectric losses.[8]

The substitution of diamagnetic ions in spinel ferrites is known to produce changes in the electrical, magnetic and micro- structural properties.[7] Furthermore, the diamagnetic substituted spinel ferrites exhibit very high-temperature environmental stability and hard mechanical characteristics.[9] MgO is known to be a stable oxide and avoids the formation of divalent iron ions and thereby increases the resistivity of material compounds.[10] The effect of Mg substitution on Ni-Cu-Zn ferrites has shown improvement in permeability and

(Received October 12, 2016; accepted May 22, 2017; published online June 5, 2017)

reduction in Curie temperature,[11] decreases in dielectric loss and increasesin AC resistivity,[12] better grain size for low-temperature sintered ferrites at higher frequency,[13] low dielectric parameters[14] and high permeability.[15]

Various methods such as ceramic, sol–gel, co-precipitation, sonochemical preparation, citrate precursor technique, micro-emulsion, etc. have been used for the preparation of various soft ferrites. With a suitable technique like auto-combustion method, it is possible to obtain high-quality materials with low losses at high frequency. The sol–gel auto- combustion method offers low cost, simplicity, short time of production and homogeneity of the final product. To the best of our knowledge, there are no reports on Mg-substituted Ni-Cu-Zn ferrites synthesized by the sol–gel auto-combustion technique. We have used glycine as the reducing agent, i.e., the fuel for the redox reaction, whereas many reports are available using other fuels in auto-combustion synthesis. We intend to reinvestigate the ferrite synthesis and the related electrical, magnetic and optical properties of the present samples.

The refractive index of any material is useful for understanding the propagation of electromagnetic radiations like IR waves in the material. At low frequencies, the dielectric permittivity may be determined by the ionic polarization, while the refractive index is determined from the electric polarization. This dispersion in terms of refractive index can be used as a detector for IR waves.[16] The optical parameters like refractive index, velocity of IR waves and jump rates of lattice vacancies are reported from FTIR spectra for the first time for Mg-substituted NiCuZn ferrites.

Very few investigations are available in the literature on the effect of magnesium substitution in place of Ni on the electromagnetic properties of M- substituted NiCuZn ferrites. In this context, the present paper is devoted to study the effect of Mg substitution for Ni on the structural, magnetic, optical, electrical and dielectric properties of $Ni_{0.25-x}Mg_xCu_{0.30}Zn_{0.45}Fe_2O_4$ ($0 \le x \ge 0.25$) ferrites. Here, we have attempted to report the electric polarization in terms of optical parameters like refractive index, velocity of IR waves and jump rates of lattice vacancies, which are determined from the IR absorption spectrum in Ni-Mg-Cu-Zn ferrites. We have also focused our attention on the change in the dimensions of the cations and their distribution over A and B sub-lattices based on the experimental observations of magnetic moments from hysteresis measurements.

EXPERIMENTAL

The metal nitrates and glycine ($C_2H_5NO_2$), which acts as a fuel (reducing agent) for the combustion reaction, form the redox mixture.[17] Glycine has a very high negative heat of combustion (−3.24 kcal/g), hence it is a proper reducing agent to carry out the redox reaction and form the metal oxide complexes. Analytic grade (Sigma Aldrich) metal nitrates such as $Mg(NO_3)_2{\cdot}6H_2O$, $Ni(NO_3)_2{\cdot}6H_2O$, $Cu(NO_3)_2{\cdot}5H_2O$, $Zn(NO_3)_2{\cdot}6H_2O$, and $(NO_3)_3{\cdot}9H_2O$ were taken in stoichiometric proportions along with glycine (H_2NCH_2COOH) from sd-fine and dissolved in distilled water to obtainthe precursor solution. The resulting solution was then heated on an electric heater until a gel was formed. The gel then ignited in a self-propagating combustion to form a fluffy loose ash. This was lightly ground and calcined at 923 K for 4 h. The pre-sintered ferrite powder was granulated, the pellets being formed by using a uniaxial hydraulic press and applying the pressure of 10 ton/m^2 for 5 min. The pellets thus prepared were then finally sintered at 1173 K for 2 h.

X-ray diffraction (XRD) analysis was carried out at room temperature by using a Rigaku Ultima IV (Japan) x-ray powder diffractometer with CuK_α (λ = 1.5406 Å) and secondary monochromator in the 2θ range of 20°–80°. The average crystallite size of the sintered powders was determined by the Scherrer formula using the line broadening width of the highest intensity peak due to the (311) plane.[18] The bulk densities were measured by the liquid immersion technique based on Archimedes' principle. Xylene was used as the liquid medium and weights were measured on a single pan digital balance. The porosities were calculated from the XRD densities (d_{XRD}) and the bulk densities (d_{bulk}). The magnetic properties were studied by using a vibrating sample magnetometer (VSM) (model 4500 EG; G Princeton Applied Research, USA) at 80 K. IR absorption spectra of Mg-substituted Ni-Cu-Zn ferrites were obtained on a Perkin-Elmer IR spectrometer in the wave number ranging from 400 cm^{-1} to 1600 cm^{-1} using the KBr pellet method. The DC electrical resistivity measurement was carried out from room temperature to 773 K using the two-probe method. The dielectric measurements were carried out using a LCR meter (Model HP-4284A) at 300 K in the frequency range 20 Hz–1 MHz.

RESULTS AND DISCUSSION

Structural Analysis

The x-ray diffraction (XRD) patterns of the $Ni_{0.25-x}Mg_xCu_{0.30}Zn_{0.45}Fe_2O_4$ ($0 \le x \le 0.25$ mol.%) system is shown in Fig. 1. The XRD patterns were indexed using JCPDS card no. 08-0234, which confirms the formation of a cubic spinel structure. Traces of unreacted Fe_2O_3 (JCPDS card no. 33-0664) were observed in the XRD pattern and may be attributed to the incomplete combustion reaction during the phase formation. This means that the Fe_2O_3 phase becomes segregated into the matrix of the spinel ferrite phase which acts as a secondary phase. The value of the lattice constant (a) decreases with the substitution of Mg content,[18]

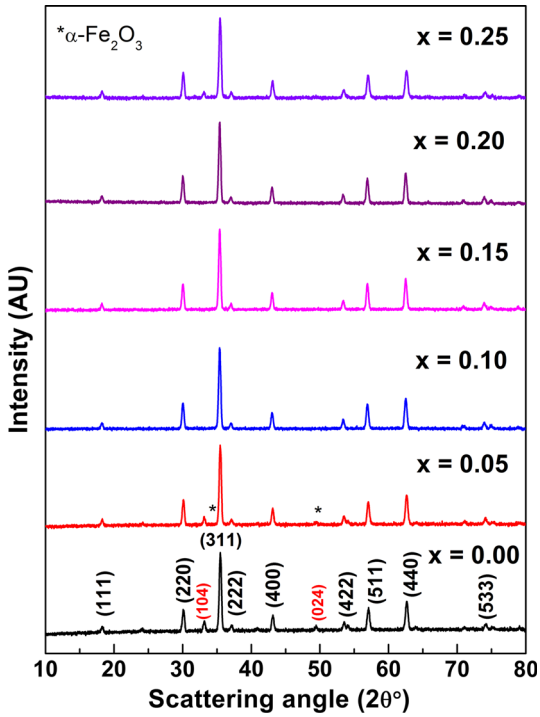

Fig. 1. XRD patterns of $Ni_{0.25-x}Mg_xCu_{0.30}Zn_{0.45}Fe_2O_4$ ferrites.

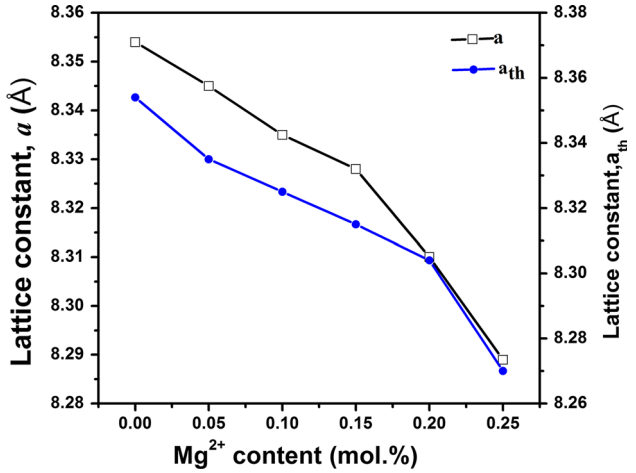

Fig. 2. Variation of lattice parameter (a) and theoretical lattice parameter (a_{th}) as a function of Mg content for $Ni_{0.25-x}Mg_xCu_{0.30}Zn_{0.45}Fe_2O_4$ ferrites.

which may be attributed to the smaller ionic radii of Mg^{2+} (0.71 Å) than that of Ni^{2+} (0.78 Å), hence Mg^{2+} enters into the crystal structure of the lattice and the size of the unit cell decreases as shown in Fig. 2.

The crystallite size (D) is found to be increased with the Mg content and reaches to a maximum value of ~33.14 nm for x = 0.25 mol.%., in line with the report by Abdullah et al.[2] The x-ray density (d_{XRD}) shows the decreasing trend with respect to Mg^{2+} substitution, which can be explained on the basis of the atomic weight of Mg^{2+} as compared to Ni^{2+}, as well as the density of Mg (1.74 gm/cm^3), which is low compared to Ni (8.91 gm/cm^3).[19] The apparent/bulk density (d_{bulk}) of $Ni_{0.25-x}Mg_xCu_{0.30}Zn_{0.45}Fe_2O_4$ ferrites was determined by the liquid immersion technique based on Archimedes' principle with xylene as the medium. The increase in porosity (P) (Table I) of each sample indicates the crystal imperfections. The difference in the two densities arises due to the pores in the crystal formation, which depends on stoichiometry, method of preparation, heat treatment conditions, etc.

Magnetic Properties

The magnetic properties such as saturation magnetization (M_S), retentivity (M_r) and coercive field (H_c) were studied by recording the magnetic hysteresis loops by using VSM, and the magnetic moment is calculated by using the following relation[20]:

$$n_B = \frac{M \times M_S}{5585} \quad (1)$$

where M is the molecular weight of the ferrite sample, 5585 is the magnetic factor and M_s is the observed saturation magnetization. The VSM measurements are carried out at the low temperature of 80 K, because at this temperature there isa more orderly alignment of spins as compared to room temperature (300 K). The hysteresis loops of the $Ni_{0.25-x}Mg_xCu_{0.30}Zn_{0.45}Fe_2O_4$ system are shown in Fig. 3. The narrow/slim magnetic hysteresis loops of the samples indicate that the ferrite samples are magnetically soft with low coercivity and possess a ferrimagnetic nature. The compositional data on x-ray density (d_{XRD}), bulk density (d_{bulk}), percentage porosity (p), saturation magnetization (M_S), remanent magnetization (M_r), anisotropy constant (K_1) and Yafet–Kittel angle (α_{Y-K}) are tabulated in Table I. The decrease in M_S can be explained on the basis of the magnetic moment of Ni^{2+} (2.3 μ_B) and Mg^{2+} (1.1 μ_B).[21] However, Mg^{2+} shows partial distribution between the A-site and the B-site, while Zn^{2+} has strong occupancy on the A-site. The values of the Bohr magneton (n_B) are found to decrease with the increase of Mg^{2+} content. This is because the A–B exchange interaction becomes strong due to the replacement of Ni^{2+} ions by Mg^{2+} ions at the respective sites.

Cation Distribution

The predictable cation distribution of the spinel ferrite (A) $[B]_2O_4$ can be represented as follows: $(Zn_{0.45}Ni_{0.1-0.4x}Mg_{0.4x}Cu_{0.10}Fe_{0.35})^A$ $[Ni_{0.15-0.6x}Mg_{0.6x}Cu_{0.20}Fe_{1.65}]^BO_4$; where x is the content of Mg^{2+}. Based on the magnetic moments of the constituent ions, the theoretical magnetic moments are calculated by considering Neel's two-sublattice model of ferrimagnetism.[22] The magnetic moment per formula unit in terms of the Bohr magneton (μ_B); n_B^N is expressed using the relationship:

Table I. The compositional data on x-ray density (d_{XRD}), bulk density (d_{bulk}), percentage porosity (P), saturation magnetization (M_S), remanent magnetization (M_r), anisotropy constant (k_1) and Yafet–Kittel angle (α_{Y-K})

Mg content (x)	d_{XRD}	d_{bulk}	P (%)	M_S (80 K) emu/gm	M_r (80 K) emu/gm	$-K_1 \times 10^4$ erg/cc	α_{Y-K} (80 K)
0.00	5.54	4.93	8.50	40.22	4.92	2.28	32°41′16″
0.05	5.52	4.84	9.84	20.18	4.10	2.29	39°36′31″
0.10	5.49	4.69	11.34	29.41	3.98	2.30	36°19′49″
0.15	5.47	4.42	12.05	27.63	3.69	2.31	35°38′27″
0.20	5.44	4.35	12.46	31.86	3.13	2.32	33°14′29″
0.25	5.39	4.28	14.46	41.05	3.99	2.33	31°46′14″

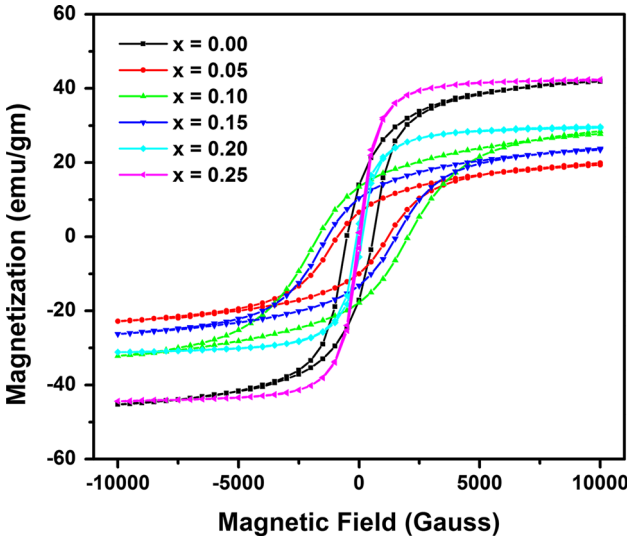

Fig. 3. Hysteresis loops of $Ni_{0.25-x}Mg_xCu_{0.30}Zn_{0.45}Fe_2O_4$ ferrites.

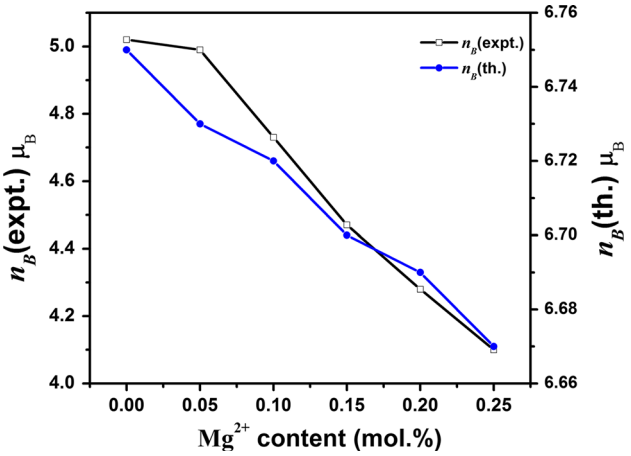

Fig. 4. Compositional variation of experimental magnetic moment (n_B) and theoretical magnetic moment (n_B) of $Ni_{0.25-x}Mg_xCu_{0.30}Zn_{0.45}Fe_2O_4$ ferrites.

$$n_B^N(x) = M_B(x) - M_A(x) \quad (2)$$

where M_B and M_A are the octahedral B-site and the tetrahedral A-site sublattice magnetic moments, respectively, in the Bohr magneton. The net theoretical magnetic moment $(n_B)(th)\mu_B$ as calculated using the magnetic moments of the cations Zn^{2+} (0 μ_B), Cu^{2+} (1.3 μ_B), Mg^{2+} (1.1 μ_B), Ni^{2+} (2.3 μ_B) and Fe^{3+} (5 μ_B). Mg^{2+} are used to substitute Ni^{2+} ions at the A-site and the B-site, keeping the Zn^{2+} ions constant. However, Zn^{2+} ions have a preference for tetrahedral sites due to their readiness to form covalent bonds involving sp^3 hybrid orbitals due to their favorable fit of charge distribution. The basic magnetic properties originate from Mg^{2+} ions, Cu^{2+} ions and Fe^{3+} ions residing both on the tetrahedral (A) and octahedral (B) sites. The compositional variation of the experimental magnetic moment (n_B) (expt) μ_B and the theoretical magnetic moment (n_B) (th)μ_B is shown in Fig. 4. The cation distribution of the ions based on the two sublattices and magnetic moments (experimental and theoretical) are given in Table II. M_S values decrease with increasing Mg^{2+} content and, at $x = 0.25$, they increase again. There is a random trend in the magnetic properties which may be attributed to the impurity phase α-Fe_2O_3. Similar variation is observed in n_B(expt) which can be observed from Eq. 1. The net magnetic moment (n_B), the Y–K angle (α_{Y-K}), the magnetic moment of sublattice A (M_A) and magnetic moment of sublattice B (M_B) are related by the expression:

$$n_B = M_B \mathrm{Cos}\,\alpha_{Y-K} - M_A \quad (3)$$

The decrease in M_S and n_B is based on Yafet–Kittel (Y–K) angle calculated from M_S and n_B as given in relationship (3).

It is observed that, with the increase of Mg^{2+} content, there is an increase in α_{Y-K} angle, hence there is additional canting at the A and B sites. The inter-sublattice super-exchange interactions of the cations on the (A–B) site are much stronger than (A–A) and (B–B) intra-sublattice exchange interactions. The preferential occupancy of Mg^{2+} ions to tetrahedral and octahedral sites in the ferrite sample results in decreasing the concentration of Fe^{3+} ions at these sites thus reducing the B–B exchange interactions and consequently reducing the (A–B) super-exchange interactions. Hence, the main contribution of magnetic properties derives from the highly magnetic Fe^{3+} ions (magnetic

Table II. The cation distribution and magnetic moments (experimental and theoretical) of the $Ni_{0.25-x}Mg_xCu_{0.30}Zn_{0.45}Fe_2O_4$ ferrite system

Mg content (x)	Cation distribution		n_B (expt) μ_B	n_B(th) μ_B
	A-site	B-site		
0.00	$(Zn^{2+}_{0.45}Ni^{2+}_{0.1}Cu^{2+}_{0.10}Fe^{3+}_{0.35})$	$\left[Ni^{2+}_{0.15}Cu^{2+}_{0.20}Fe^{3+}_{1.65}\right]O^{2-}_4$	5.02	6.74
0.05	$(Zn^{2+}_{0.45}Ni^{2+}_{0.08}Mg^{2+}_{0.02}Cu^{2+}_{0.10}Fe^{3+}_{0.35})$	$\left[Ni^{2+}_{0.12}Mg^{2+}_{0.03}Cu^{2+}_{0.20}Fe^{3+}_{1.65}\right]O^{2-}_4$	4.47	6.73
0.10	$\left(Zn^{2+}_{0.45}Ni^{2+}_{0.06}Mg^{2+}_{0.04}Cu^{2+}_{0.10}Fe^{3+}_{0.35}\right)$	$[Ni^{2+}_{0.09}Mg^{2+}_{0.06}Cu^{2+}_{0.20}Fe^{3+}_{1.65}]O^{2-}_4$	4.73	6.72
0.15	$\left(Zn^{2+}_{0.45}Ni^{2+}_{0.04}Mg^{2+}_{0.06}Cu^{2+}_{0.10}Fe^{3+}_{0.35}\right)$	$\left[Ni^{2+}_{0.06}Mg^{2+}_{0.09}Cu^{2+}_{0.20}Fe^{3+}_{1.65}\right]O^{2-}_4$	4.62	6.70
0.20	$\left(Zn^{2+}_{0.45}Ni^{2+}_{0.02}Mg^{2+}_{0.08}Cu^{2+}_{0.10}Fe^{3+}_{0.35}\right)$	$\left[Ni^{2+}_{0.03}Mg^{2+}_{0.12}Cu^{2+}_{0.20}Fe^{3+}_{1.65}\right]O^{2-}_4$	4.48	6.69
0.25	$\left(Zn^{2+}_{0.45}Mg^{2+}_{0.10}Cu^{2+}_{0.10}Fe^{3+}_{0.35}\right)$	$\left[Mg^{2+}_{0.15}Cu^{2+}_{0.20}Fe^{3+}_{1.65}\right]O^{2-}_4$	5.09	6.67

moment is fixed at +5 μ_B) {spin only} present in the B-sites. The successive replacement of Fe^{3+} ions by Mg^{2+} ions decreases the Fe^{3+}-Fe^{3+} (B–B) interaction.[3] The coercivity of the ferrites represents the strength of the magnetic field which is necessary to surpass the anisotropy barrier and allow the magnetization of the nanoparticles following the magnetic field orientation. The coercivity field (H_C) increases with the content of Mg^{2+} for $x \le 0.15$. Porosity influences the magnetization process because the pores work as a generator of the demagnetizing field. As the porosity value increases, a higher field is needed to push the domain wall, thereby increasing H_C. A crystalline field distortion can lead to internal stress contributing to the anisotropy.[23] By considering the appropriate stoichiometry of the composition of the ferrites and the theoretical end values of the anisotropy constant (K_1) for $MgFe_2O_4$[23] (-2.5×10^4 erg/cm^3) and for $NiFe_2O_4$[23] (-2.8×10^3 erg/cm^3), the anisotropy constants (K_1) of the ferrite samples were calculated.

It is well reported that there is correlation between the ionic radii of both A and B interstitial lattice sites of a spinel structure. The values of the theoretical lattice parameter (a_{th}) were calculated using the formula[24]:

$$a_{th} = \frac{8}{3\sqrt{3}}\left[(r_A + r_0) + \sqrt{3}(r_B + r_0)\right] \quad (4)$$

where r_o is the radius of the oxygen ion (1.33 Å)[22] and r_A, r_B are the ionic radii of the tetrahedral and octahedral sites, respectively. The values of r_A and r_B depend on the cation distribution of the ferrite system.[20,24] Based on the site occupancy of the cations reported, the possible cation distribution is proposed which explains the spin alignment of the ferrites. The broad bands at the A-site and the B-site justify the cation distribution. Table II shows the cation distribution of the various compositions of Mg-substituted Ni-Cu-Zn ferrites and is based on Neel's two-sublattice model[20]; in which Zn^{2+} ions have a strong tendency to occupy the A-sites, while Ni^{2+} ions have a strong preference to occupy the B-sites[25–27] and Mg^{2+}, Cu^{2+}, Fe^{3+} ions can exist at both the A-site and the B-site.[28]

Table III shows the lattice constant(a), tetrahedral site radius (r_A), octahedral site radius (r_B), theoretical lattice constant (a_{th}), molecular weight on the A-site (M_A), molecular weight on the B-site (M_B), bond length (L_A) and bond length (L_B) with content of Mg^{2+}. The ionic radii of the A site (r_A) and B-site (r_B) based on the cation distribution of Mg-substituted Ni-Cu-Zn ferrite were calculated theoretically[29,30] as follows:

$$r_A = C_{AZn}r(Zn^{2+}) + C_{ACu}r\left(Cu^{2+}\right) + C_{AMg}r(Mg^{2+}) + C_{AFe}r(Fe^{2+}) \quad (5)$$

$$r_B = 1/2\left[C_{BNi}r(Ni^{2+}) + C_{BCu}r\left(Cu^{2+}\right) + C_{BMg}r(Mg^{2+}) + C_{BFe}r(Fe^{2+})\right] \quad (6)$$

where $r(Zn^{2+})$ = 0.82 Å, $r(Mg^{2+})$ = 0.71 Å, $r(Fe^{2+})$ = 0.67 Å, $r(Cu^{2+})$ = 0.70 Å and $r(Ni^{2+})$ = 0.78 Å.[22] C_{AZn},C_{AMg} and C_{AFe} are the corresponding ion concentrations at the A-sites and C_{BNi}, C_{BMg}, C_{BCu} and C_{BFe} are the corresponding ion concentrations at the B-sites. Using the values of r_A and r_B, the theoretical lattice parameter (a_{th}) was calculated. The decrease in a_{th} with the increase in Mg^{2+} is attributed to the difference of ionic radii Mg^{2+} (0.71 Å) and Ni^{2+} (0.78 Å), and hence there is partial replacement of the Ni^{2+} ions by Mg^{2+} ions. It is therefore suggested that most of the replacement of Ni^{2+} ions by Mg^{2+} ions takes place on the octahedral site.[26] A-site and B-site bond lengths (L_A and L_B) are calculated and it is observed that L_A and L_B decrease with increasing content of Mg^{2+}, which is similar to the lattice parameter variation trend. This is because the ionic radius of Mg^{2+} is smaller than that of Ni^{2+}. The difference between a and a_{th} can be attributed to the presence of Fe^{2+} ions at the B-sites and other crystal imperfections.

Table III. The compositional data on lattice parameter (a), tetrahedral site radius (r_A), octahedral site radius (r_B), theoretical lattice parameter (a_{th}), molecular weight (M_A), molecular weight (M_B), bond length (L_A) and bond length (L_B) of the $Ni_{0.25-x}Mg_xCu_{0.30}Zn_{0.45}Fe_2O_4$ ferrite system

Mg content (x)	a Å	r_A Å	r_B Å	a_{th} Å	M_A a.m.u.	M_B a.m.u.	L_A Å	L_B Å
0.00	8.358	0.752	0.681	8.378	327.590	756.718	7.235	4.177
0.05	8.335	0.750	0.680	8.368	326.638	755.680	7.231	4.175
0.10	8.310	0.748	0.679	8.349	325.685	754.641	7.231	4.175
0.15	8.300	0.747	0.678	8.328	324.733	753.600	7.224	4.171
0.20	8.296	0.745	0.677	8.299	323.790	752.561	7.209	4.162
0.25	8.285	0.744	0.676	8.267	322.838	751.520	7.178	4.145

FTIR Studies

Fourier-transform infrared (FTIR) spectroscopy is a versatile characterization tool used to (1) study different types of absorption bands in the spectrum, (2) determine the local symmetry in crystalline solids, ordering phenomenon,and the presence/absence of Jahn–Teller ions, and (3) determine force constants of crystalline solids.[16] Figure 5 shows representative room temperature FTIR spectra for Mg-Ni-Cu-Zn ferrites. The spectra exhibit two characteristic absorption bands in the wave number range from 400 cm^{-1} to 1600 cm^{-1}. Table IV shows the data on tetrahedral frequency (υ_1), octahedral frequency (υ_2), threshold frequency (υ_{th}), threshold energy (E_{th}), tetrahedral force constant (k_t) and octahedral force constant (k_o) for the Ni-Mg-Cu-Zn ferrites. A tetrahedral band (υ_1) and an octahedral band (υ_2) are observed as the two prominent absorption bands from the IR spectrum. The difference in the positions of the bands arises due to difference in the distances for the tetrahedral ions and octahedral ions.[31] The high-frequency band υ_1 lies in the range 712–719 cm^{-1}, while the low-frequency band υ_2 lies between 412 cm^{-1} and 440 cm^{-1}. According to the study of vibration spectra by Waldron,[32] the υ_1 band arises due to the intrinsic vibrations of the tetrahedral group and the υ_2 band arises due to the intrinsic vibrations of the octahedral group. The change in the band positions of υ_1 and υ_2 is because of the change in the bond length of Fe^{3+}-O^{2-} at the A-sites (0.189 nm) and the B-sites (0.199 nm), respectively.[33] The bands υ_1 and υ_2 varying with Mg substitution are affected by the method of preparation and sintering temperature.[34] In an inverse spinel structure, the bands υ_1 and υ_2 are broad in which Fe^{3+} ions are distributed statistically at tetrahedral and octahedral sites depending on the stoichiometry.[35] The band υ_1 decreases with increasing Mg substitution which is due to the decrease in unit cell (a) dimensions, resulting in a decrease of bond length. The octahedral frequency band υ_2 decreases due to Mg^{2+} (0.71 Å) replacing Ni^{2+} (0.78 Å) at the octahedral sites and this pushes Fe^{3+} ions towards O^{2-} ions which gives a reduction in the bond length. The force constant is a second-order derivative of potential energy with respect to the site radius (r_A and r_B), the other independent parameters being kept constant. It receives its major contribution from short-order closed-shell repulsive forces rather than from coulomb attractive forces at the ionic equilibrium positions. The force constant will therefore be more sensitive to a decrease in bond length than to an increase. The compositional variations of the tetrahedral force constant (k_t) and the octahedral force constant (k_o) are shown in Fig. 6. The threshold frequency υ_{th} for the electronic transition can be determined from the maximum point of absorption spectra, where it reaches a limiting value as shown in Fig. 5. For the electronic transition, the inflection point (Fig. 5) of transmittance versus wave number was chosen as the threshold frequency υ_{th}. From the Planck's quantum theory of radiation, threshold energy E_{th} values are calculated by using the equation $E_{th} = h\upsilon_{th}$, where h is Planck's constant and υ_{th} is the threshold frequency in cm^{-1}. The values of υ_{th} and E_{th} are in good agreement with those reported for the mixed Ni-Zn ferrite.[32] The υ_{th} arises due to electronic transition and is found to shift towards the lower frequency side with the increasing concentration of Fe^{3+} ions in the spinel ferrites. The observed decrease in the lattice parameter value and shifting of the υ_{th} band towards a lower frequency can be explained as due to the increasing concentration of ferrous (Fe^{2+}) ions at the B-site of the spinel lattice. Thus, electron hopping between ferrous (Fe^{2+}) and ferric (Fe^{3+}) ions on the octahedral complex given by $Fe^{2+} \leftrightarrow Fe^{3+} + e^-$ is enhanced. A decrease in energy for electronic transition (υ_{th}) due to the increasing content of Mg^{2+} causes a shift of threshold energy (E_{th}) towards a lower frequency.[33] For the tetrahedral A-site, the half band width (Γ_A) is calculated by the method of full width at half maximum (FWHM). With increasing content of Mg^{2+}, the half band width Γ_A decreases and the broadening of the band is commonly observed. As reported earlier, when the system transfers from an inverse spinel to a normal spinel structure, there is a broadening of the bands. This broadening arises due to the statistical distribution of the Fe^{3+} ions at the A-sites and the B-sites. In the present system, we observe from the cation

distribution that more divalent metal ions (Mg^{2+}) occupy the B-sites and due to perturbation more inverse spinel structure results.

Optical Properties

The refraction index (η) and the velocity of the IR radiation (υ) in the ferrite material were evaluated using the relationships[16,36,37] : $\frac{E_{trans}}{E_{ab}} = c/\upsilon = \eta$, where E_{ab} (absorbed energy) = $hc\upsilon_1$, E_{trans}(transmitted energy) = $hc\upsilon_{th}$, $E_{ab} = hc\upsilon_1$, $E_{ab} = hc\upsilon_2$, where υ is velocity of light in the medium, (υ_1, υ_2 and υ_{th}) are tetrahedral, octahedral and threshold frequencies in m^{-1}, and c is the velocity of light.

The degree of bending or the magnitude of η depends on the wavelength of the incident radiation and decreases with increasing wavelength.[37] The tetrahedral site refractive index (η_1) and octahedral site refractive index (η_2) are calculated corresponding to the principle of IR absorption bands υ_1 and υ_2, respectively. The average refractive index (η) is further used to calculate the velocity of IR radiations (υ) and reflectivity (R). Finally, the tetrahedral jump rate (J_1), octahedral jump rate (J_2) and average jump rate (J)[16,38] of the charge carrier (i.e. electron) is calculated using given relationships as:

$$R = \left(\frac{\eta-1}{\eta+1}\right)^2, J_1 = f_1 e^{-E_1/(k_B T)}, J_2 = f_2 e^{-E_2/(k_B T)},$$

$$J = \frac{J_1 + J_2}{2}$$

where f_1 is the A-site frequency vibration and f_2 is the B-site frequency vibration, k_B is the Boltzmann constant, T = 300 K, $E_1 = hf_1 = h\upsilon_1$ and $E_2 = hf_2 = h\upsilon_2$, where h is the Planck's constant.

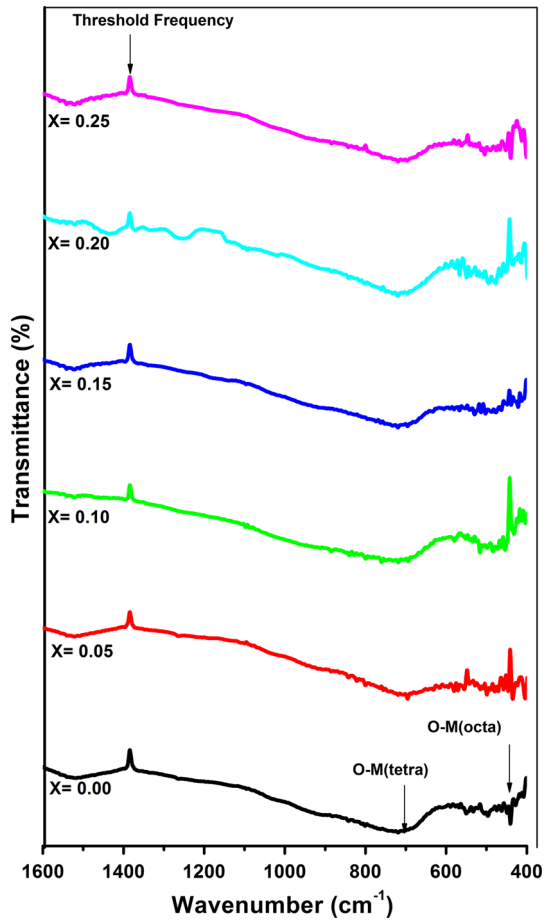

Fig. 5. FTIR spectra for $Ni_{0.25-x}Mg_xCu_{0.30}Zn_{0.45}Fe_2O_4$ ferrites.

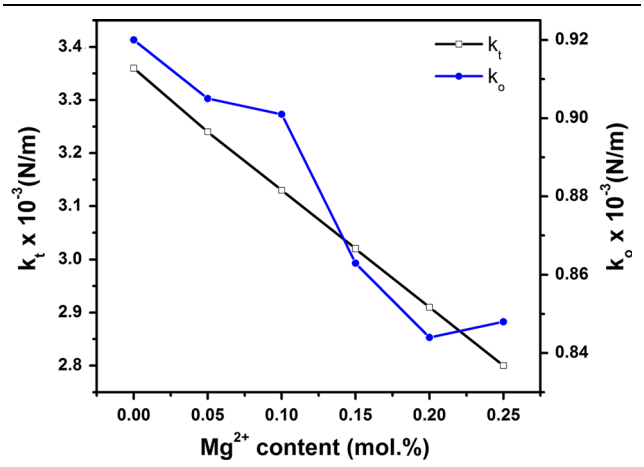

Fig. 6. Variation of tetrahedral force constant (k_t) and octahedral force constant (k_o) for $Ni_{0.25-x}Mg_xCu_{0.30}Zn_{0.45}Fe_2O_4$ ferrites.

Table IV. Data on tetrahedral frequency band (υ_1), octahedral frequency band (υ_2), threshold frequency (υ_{th}), threshold energy (E_{th}), tetrahedral force constant (k_t) and octahedral force constant (k_o) of $Ni_{0.25-x}Mg_xCu_{0.30}Zn_{0.45}Fe_2O_4$ ferrite system

Mg content (x)	$\upsilon_1 \times 10^{-2}$ m^{-1}	$\upsilon_2 \times 10^{-2}$ m^{-1}	$\upsilon_{th} \times 10^{-2}$ m^{-1}	E_{th} eV	$k_t \times 10^{-3}$ Nm^{-1}	$k_o \times 10^{-3}$ Nm^{-1}
0.00	719	440	1383	0.1714	3.41	0.92
0.05	717	435	1380	0.1709	3.28	0.91
0.10	716	431	1378	0.1707	3.19	0.89
0.15	715	421	1375	0.1703	3.06	0.86
0.20	713	413	1373	0.1701	2.91	0.84
0.25	712	412	1371	0.1697	2.76	0.82

Table V. Data on half band width (Γ_A), velocity of IR waves (v), refractive indices (η_1, η_2, η), reflectivity (R), jump rates (J_1, J_2, and J) of the $Ni_{0.25-x}Mg_xCu_{0.30}Zn_{0.45}Fe_2O_4$ ferrite system

Mg content (x)	$\Gamma_A \times 10^{-2}$ m^{-1}	$v \times 10^8$ m s^{-1}	η_1	η_2	η	R	$J_1 \times 10^9$ Hz	$J_2 \times 10^9$ Hz	$J \times 10^9$ Hz
0.00	99.41	1.200	1.923	3.139	2.531	0.187	2729.7	2609.3	2669.5
0.05	95.62	1.177	1.924	3.174	2.549	0.190	2739.5	2601.6	2663.5
0.10	90.12	1.172	1.924	3.197	2.560	0.192	2741.1	2577.5	2659.3
0.15	85.36	1.157	1.925	3.262	2.592	0.196	2749.0	2546.9	2647.9
0.20	80.17	1.144	1.925	3.320	2.622	0.200	2750.0	2517.9	2633.9
0.25	73.12	1.144	1.925	3.320	2.621	0.200	2751.0	2510.7	2630.8

Table V shows the data on half band width (Γ_A), velocity of IR waves (v), refractive indices (η_1, η_2, η), reflectivity (R), and jump rates (J_1, J_2, J) for varying with the content of Mg.

The retardation of electromagnetic radiations in the medium gives rise to electronic polarization. The constituent atom size or ions has a considerable influence on the magnitude of this retardation; generally, the larger the ion or atom, the greater the electronic polarization, the slower the velocity of infra-red rays and the greater the refractive index.[38] The reflectivity is directly proportional to the index of refraction of the solid because, when the electromagnetic radiation is transmitted from vacuum/air into a solid, a fraction of the electromagnetic radiation is reflected at the interface between the two media. Since the refractive index of air is nearly equal to unity, the higher the refractive index of the solid, the greater the reflectivity. The reflectivity was found to vary from 18.7% to 20% with the content of Mg. As the content of Mg^{2+} increases,the jump rate (J) decreases since there is an increase in anion vacancies produced by the formation of ferrous (Fe^{2+}) ions in the lattice.[16,39]

Electrical Transport

The DC electrical resistivity (ρ_{DC}) is an important parameter of low-temperature sintered ferrites used in MLCI applications, because resistivity remarkably affects the electroplating of the devices. DC resistivity (ρ_{DC}) is determined by using a two-probe method. The thermal variation of $\log\rho_{DC}$ versus ($1000/T$) for various compositions is shown in Fig. 7. The thermal variation is almost linear up to the Curie temperature (T_C), but a break occurs in the transition point of magnetic ordering from ferrimagnetism to paramagnetism, i.e. the permanent magnetization changes to induced magnetization at T_C.[40–42] The Curie temperature (T_C) values are determined from Fig. 7 for various compositions of Mg^{2+} and were found to vary from 446 K to 418 K for $0.00 \le x \le 0.25$. These values are in good agreement with the Curie temperatures reported by Penchal Reddy et al.[42] for $Ni_{0.35}Cu_{0.05}Zn_{0.60}Fe_2O_4$ ferrites. The Curie temperatures of $NiFe_2O_4$ and of $MgFe_2O_4$ are 858 K and 713 K, respectively, and the substitution of Ni^{2+} by Mg^{2+} shows a decrease in Curie temperature. This is due to the interaction between the A and B sublattices. Hence, the thermal energy required to offset the spin alignment decreases, thereby decreasing the Curie temperature. The low-temperature region arises due to a conduction process of extrinsic-type carriers and the high-temperature region arises due to the hopping of polarons. The Verwey mechanism can be used to explain the conduction mechanism in ferrites. A fractional amount of Fe^{2+} and Ni^{3+} ions is formed during the sintering process, and the electron exchange is believed to be inbetween the iron ions and the nickel ions, which can be shown as $Ni^{2+} + Fe^{3+} \rightarrow Fe^{2+} + Ni^{3+}$.[43] Hopping of electrons between trivalent and divalent ions within the octahedral positions without a change in the energy state of a crystal leads to the conduction mechanism. As the divalent ion increases, the resistivity decreases. Here, the conduction is attributed to the transfer of electrons between the ions, and these ions have a random distribution on crystallographic equivalent lattice sites. The separation between two metal ions present at the B-site is smaller than the separation between metal ions on the octahedral and tetrahedral sites. Hence, the probability of electron hopping between the octahedral and tetrahedral sites is small as compared to the ions present at the octahedral sites only. This hopping mechanism depends on the distance between the metal ions and the mobility of the charge carriers. The maximum DC resistivity (1.52×10^6 Ω-cm) is observed for the ferrite $Ni_{0.10}Mg_{0.15}Cu_{0.30}Zn_{0.45}Fe_2O_4$ at room temperature. The resistance of the ferrite is controlled by Fe^{2+} concentration on the octahedral B-site; hence, conduction takes place through hopping of electrons between trivalent and divalent ions, which is confirmed by the variation of resistivity with temperature. The DC electrical resistivity (ρ_{DC}) depends on temperature and is given by the Arrhenius relationship[40]:

$$\rho_{DC} = \rho_0 \exp\left(\frac{E_a}{K_B T}\right) \quad (7)$$

where ρ_0 is the temperature-independent constant, E_a is the energy of activation, k_B is Boltzmann's constant and T is the absolute temperature. The activation energies can be calculated using the

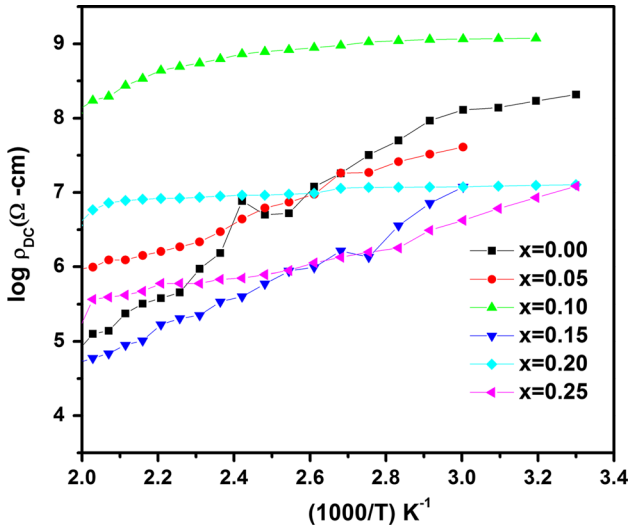

Fig. 7. Variation of DC resistivity (logρ_{DC}) with temperature for $Ni_{0.25-x}Mg_xCu_{0.30}Zn_{0.45}Fe_2O_4$ ferrites.

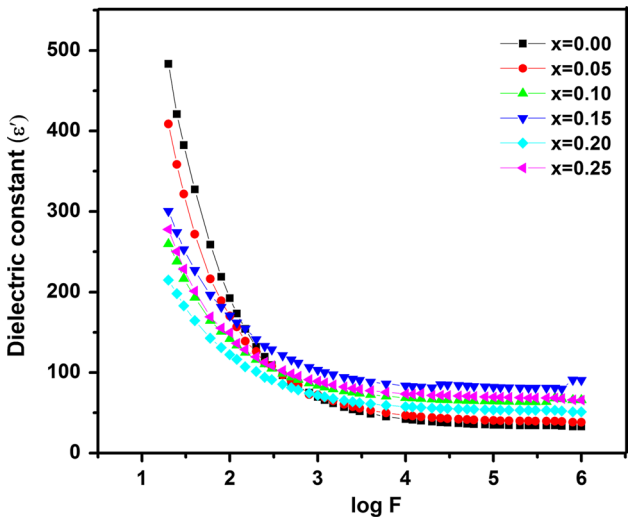

Fig. 8. Variation of dielectric constant (ε') with log frequency for $Ni_{0.25-x}Mg_xCu_{0.30}Zn_{0.45}$ Fe_2O_4 ferrites.

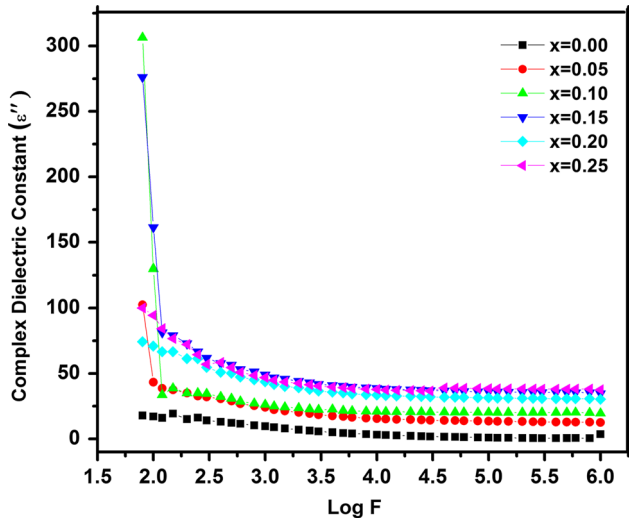

Fig. 9. Variation of complex dielectric constant (ε'') with log frequency for $Ni_{0.25-x}Mg_xCu_{0.30}Zn_{0.45}Fe_2O_4$ ferrites.

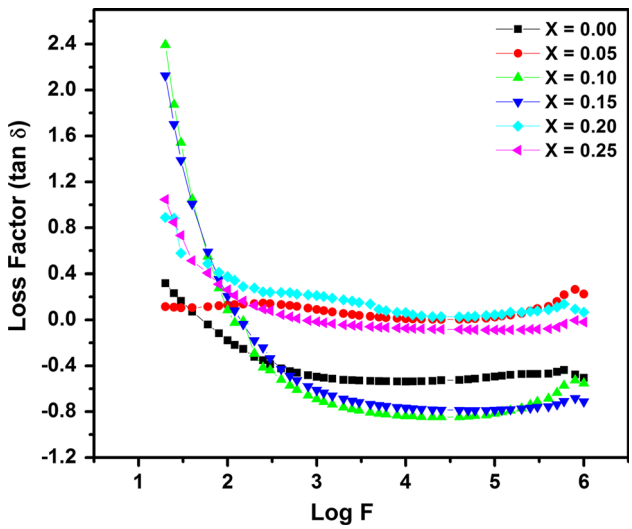

Fig. 10. Variation of dielectric loss tangent (tan δ) with log frequency for $Ni_{0.25-x}Mg_xCu_{0.30}Zn_{0.45}Fe_2O_4$ ferrites.

Arrhenius relationship. The activation energies in the ferrimagnetic region (ΔE_f) lie in the range 0.1899–0.2394 eV, and the activation energies in the paramagnetic region (ΔE_p) lie in the range 0.2715–0.3521 eV. At the Curie temperature (T_C), magnetic ordering transition changes from the ferrimagnetic to the paramagnetic region. At the transition point, there is an exchange interaction between the inner and outer electrons of the ions at the A–B sublattice. In the ferrimagnetic region, the values of ΔE_f are smaller and are in low-temperature range arising due to impurity ions. In the paramagnetic region, the values of ΔE_p are larger and are in the high-temperature range arising due to polaron hopping. The activation energies above the Curie temperature indicate the electron hopping of Mg^{2+} ions.[21] The resistivity of the ferrite samples decreases with the increase in temperature, indicating the semiconductor nature of the material. With the increase in temperature, the resistivity decreases due to the increase in drift mobility of the charge carriers.[41]

An impurity peak of α-Fe_2O_3 is observed which may be attributed to the incomplete combustion reaction during phase transformation; further Fe_2O_3 is a conducting oxide and hence dilutes the resistivity of the material. However due to phase segregation of Fe_2O_3 a random trend is observed in the variation of DC resistivity with Mg content. $NiFe_2O_4$ has electrical resistivity 0.5×10^9 Ω-cm and $MgFe_2O_4$ has electrical resistivity 0.5×10^9 Ω-cm. Hence the substitution of Ni by Mg shows an

Table VI. Data on Curie temperatures (T_C), DC resistivity (ρ_{DC}), ferromagnetic energy (ΔE_f), paramagnetic energy (ΔE_p), dielectric constant (ε'), dielectric loss tangent ($\tan\delta$), AC Resistivity (ρ_{AC}) of the $Ni_{0.25-x}Mg_xCu_{0.30}Zn_{0.45}Fe_2O_4$ ferrite system

Mg content (x)	Curie Temperature T_C K	DC resistivity (ρ_{DC}) × 10^6 Ω-cm	Ferrimagnetic energy ΔE_f (eV)	Paramagnetic energy ΔE_p (eV)	Dielectric Constant ε' at 1 kHz	Dielectric loss factor $\tan\delta$	AC resistivity (ρ_{AC}) × 10^6 Ω-cm at 1 kHz
0.00	719	0.73	0.2196	0.2961	23.219	0.415	7.259
0.05	713	0.85	0.2394	0.3163	21.315	0.210	9.900
0.10	707	0.99	0.2493	0.3446	24.311	0.099	10.169
0.15	704	1.52	0.1899	0.3521	45.725	0.021	27.029
0.20	699	1.43	0.2364	0.2917	40.060	0.155	1.064
0.25	691	1.03	0.2168	0.2715	43.499	0.346	1.181

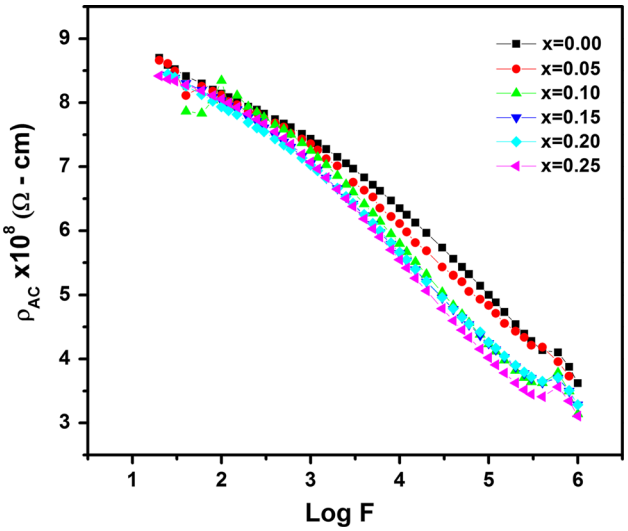

Fig. 11. Variation of AC resistivity log (ρ_{AC}) with log frequency for $Ni_{0.25-x}Mg_xCu_{0.30}Zn_{0.45}Fe_2O_4$ ferrites.

increase in electrical resistivity. High activation energies indicate higher electrical resistivity. The porosities (8–14%) indicate crystal imperfections which depend on stoichiometry, method of preparation, heat treatment conditions etc. The crystal imperfections have an intrinsic effect on the electrical properties.

Dielectric Properties

The dielectric constant ε' of the ferrite samples was calculated by using the $\varepsilon' = \frac{c_p t}{\varepsilon_0 A}$ relationship,[43] where t is the thickness of the pellet in cm, c_p is the capacitance in F, A is the area of cross-section of the specimen and ε_o is free space permittivity (8.854×10^{-12} F/m). The complex part of the dielectric constant (ε'') of the ferrite samples was calculated by $\varepsilon'' = \varepsilon' \tan\delta$, where $\tan\delta = 1/Q$ and Q is the quality factor. Variation of dielectric constant (ε') with log frequency in Hz is shown in Fig. 8. Variation of complex dielectric constant (ε'') with log frequency in Hz is shown in Fig. 9. For the Mg-substituted Ni-Cu-Zn ferrites, dielectric constants (ε' and ε'') decrease with the increase in frequency. This observed dielectric response can be explained based on the space charge polarization theory and hopping model.[44] The presence of Fe^{3+} and Fe^{2+} ions make the ferrite material exhibit dipolar polarization. The dielectric polarization is also affected by the structural homogeneity, stoichiometry and porosity of the ferrites. The rotational displacement of the dipole results in the orientation of polarization. In ferrites, exchange of Fe^{2+} to Fe^{3+} and vice versa can be obtained as the exchange of electrons between two ions, hence the dipoles align themselves. At lower frequencies, polarization is due to electron hopping between $Fe^{3+} \leftrightarrow Fe^{2+}$ ions. With increasing frequency, the polarization decreases

and attains a constant value, since beyond a certain frequency of external field, the electron exchange $Fe^{3+} \leftrightarrow Fe^{2+}$ cannot respond to the changes in the applied field. Also, due to the presence of Ni^{3+}/Ni^{2+} ions, it gives rise to *p*-type carriers and these carriers contribute to the net polarization, though it is small. The net polarization increases at the initial stage and then decreases with increasing frequency. The ferrite with the composition $x = 0.15$ exhibits a maximum dielectric constant $\varepsilon' = 45.725$ at 1 kHz because of the presence of a higher concentration of Fe^{2+} ions. The presence of these ions in the ferrite and their displacement with the applied electric field is responsible for the polarization and the increase in the dielectric constant.[15,45] The dielectric properties in the ferrite system can be explained on the basis of Maxwell–Wagner-type interfacial polarization which is in good agreement with Koop's phenomenological theory.[42,44]

Figure 10 shows the variation of the dielectric loss tangent ($\tan\delta$) as a function of log frequency in Hz for all the ferrite samples. The dielectric loss factor decreases with increasing frequency, and this is a normal behavior of any ferrite material. The dielectric loss factor decreases rapidly in the low-frequency region while the rate of decrease of dielectric loss is slow in the high-frequency region, and it shows frequency-independent behavior in the high-frequency region. The minimum dielectric loss tangent (2%) is observed for the ferrite composition $x = 0.15$, while for $x = 0.25$, there is increase in the dielectric loss tangent; hence a random trend is seen. This shows the potential of the samples for high-frequency MLCI applications.[46] Table VI shows data on Curie temperature (T_C), DC resistivity (ρ_{DC}), ferrimagnetic energy (ΔE_f), paramagnetic energy (ΔE_p), dielectric constant (ε'), dielectric loss factor ($\tan\delta$), and AC resistivity (ρ_{AC}) at 1 kHz Mg-substituted NiCuZn ferrites.

AC Resistivity (ρ_{AC})

The AC resistivity (ρ_{AC}) in Ω-cm is calculated using the relationship $\rho_{AC} = \frac{RA}{t}$, where R is the resistance of the specimen in Ω, A is the area of the cross-section and t is the thickness of the ferrite sample. At room temperature, the variation of AC resistivity (ρ_{AC}) with log frequency in Hz is shown in Fig. 11. In all the ferrite samples, ρ_{AC} decreases with increasing frequency, supporting the semiconductor behavior. When the applied frequency increases, there is an increase in probability that an electron jumps through the $Fe^{3+} \leftrightarrow Fe^{2+}$ ions. The increased content of Fe^{2+} ions induces electron hopping $Fe^{3+} \leftrightarrow Fe^{2+}$ at the B-site and hence the resistivity decreases. The inverse relationship of dielectric constant with the square root of resistivity is observed. AC resistivity decreases with frequency in disordered crystallites. According to the hopping model, at low frequency, the resistivity remains constant and here the transport takes place on infinite paths, and the resistivity decreases with the increase in the frequency because the transport is dominated by the hopping of infinite clusters. Here, the conduction mechanism is due to the hopping of electrons between two Fe^{3+}/Fe^{2+} ions at the octahedral B-site as in the present inverse spinel lattice. The AC resistivity ρ_{AC} for $x = 0.15$ is observed to be 27.029×10^6 Ω-cm at 1 kHz ,and this shows the existence of divalent iron ions at that content of Mg^{2+}.[47]

CONCLUSION

Mg-substituted Ni-Cu-Zn ferrite powders having a cubic spinel structure were successfully synthesized by the sol–gel auto–combustion process. The lattice parameter decreases with Mg substitution which can be attributed to the smaller ionic radius of Mg^{2+} compared with Ni^{2+}. The saturation magnetization and magnetic moments exhibit random trends with the increase in Mg content. The $\alpha_{Y\text{-}K}$ angles show canting and super-exchange interaction between the A–B lattice sites. The magnetic moment (theoretical and observed) values are in good agreement. The IR bands at the A-site and the B-site are broad, showing an inverse spinel structure due to statistical distribution of Fe^{3+} at the tetrahedral and octahedral sites. From FTIR, the values of υ_1 and υ_2 are found to decrease with Mg^{2+} substitution because of the reduction in the bond length. With the substitution of Mg^{2+}, the velocity of IR radiations decreases whereas the refractive index and reflectivity increase and, furthermore, the jump rate is found to decrease. The decrease of the jump rate of cation vacancies is ascribed to the filling of these vacancies by introducing Mg^{2+} ions into the lattice structure. The change in the refractive index can be used as a sensor for IR radiations. The variation in DC electrical resistivity is explained based on Verwey's hopping mechanism. Decreases in Curie temperatures indicate the substitution of Ni^{2+} by Mg^{2+} ions in the ferrite samples. Dielectric properties of the ferrite samples showed Maxwell–Wagner-type interfacial polarization. The tuning of properties of NiCuZn ferrites using Mg^{2+} dopant indicates their possible use in multilayer chip inductor (MLCI) components.

ACKNOWLEDGEMENTS

S.M. Kabbur would like to acknowledge the Instrumentation center, Solapur University, Solapur, for providing the XRD facility. R.C. Kambale thankfully acknowledges the Indian Space Research Organization (ISRO-UoP) Space Technology Cell, Government of India (Grant No. GOI-A-337 (B) (137)), and BCUD, Savitribai Phule Pune University (Grant No. RG-31) for providing research funding.

REFERENCES

1. S.E. Shirsath, R.H. Kadam, S.M. Patange, M.L. Mane, A. Ghasemi, and A. Morisako, *Appl. Phys. Lett.* 100, 042407 (2012).

2. M.D. Abdullah, V. Verma, S.P. Gairola, R.K. Singh, W.A. Siddiqui, and R.K. Kotnala, *Appl. Surf. Sci.* 258, 5342 (2012).
3. V. Chaudhari, S.E. Shirsath, R.H. Kadam, M.L. Mane, S.B. Shelke, and D.R. Mane, *J. Alloys Compd.* 549, 213 (2013).
4. H. Su, X. Tang, H. Zhang, L. Jia, and Z. Zhong, *J. Magn. Magn. Mater.* 322, 1779 (2010).
5. P. Samoila, T. Slatineanu, P. Postolache, A.R. Jordan, and M.N. Palamaru, *Mater. Chem. Phys.* 136, 241 (2012).
6. S.E. Shirsath, Y. Yasukawa, A. Ghasemi, X. Liu, and A. Morisako, *J. Appl. Phys.* 115, 17A515 (2014).
7. S.M. Kabbur, U.B. Deshmukh, S.S. Suryavanshi, and S.R. Sawant, *J. Electron. Mater.* 29, 979 (2000).
8. K.M. Akther Hossain, T.S. Biswas, T. Yanagida, H. Tanaka, H. Tabata, and T. Kawai, *Mater. Chem. Phys.* 120, 461 (2010).
9. X.W. Qi, J. Zhou, Y. Zhenxing, G. ZhiLun, and L. Long-Tu, *J. Magn. Magn. Mater.* 251, 316 (2002).
10. M.A. Gabal, *J. Magn. Magn. Mater.* 321, 3144 (2009).
11. N. Varalaxmi, N.R. Reddy, M.V. Ramana, E. Rajagopal, V.R. Murthy, and K.V. Sivakumar, *J. Mater. Sci. Mater. Electron.* 19, 399 (2008).
12. P.K. Roy and J. Bera, *J. Magn. Magn. Mater.* 298, 38 (2006).
13. M.R. Barati, *J. Sol-Gel Sci. Technol.* 52, 171 (2009).
14. C. Sujatha, K. Venugopal Reddy, K. SowriBabu, A.R. Reddy, and K.H. Rao, *Phys. Condens. Matter. B* 407, 1232 (2012).
15. C. Sujatha, K. Venugopal Reddy, K. Sowri Babu, A. Ramachandra Reddy, M. Buchi Suresh, and K.H. Rao, *J. Magn. Magn. Mater.* 340, 38 (2013).
16. O.M. Hemeda, *J. Magn. Magn. Mater.* 281, 36 (2004).
17. M.S. Khandekar, R.C. Kambale, S.S. Latthe, J.Y. Patil, P.A. Shaikh, N. Hur, and S.S. Suryavanshi, *Mater. Lett.* 65, 2972 (2011).
18. H.E. Scherrer, H. Kisker, H. Kronmuller, and R. Wurschum, *Nanostruct. Mater.* 6, 533 (1995).
19. B.D. Cullity, *The Elements of x-ray Diffraction* (London: Addison- Wesley Pub. Co. Inc., 1956), p. 42.
20. M.Y. Lodhi, K. Mahmood, A. Mahmood, H. Malik, M.F. Warsi, I. Shakir, M. Asghar, and M.A. Khan, *Curr. Appl. Phys.* 14, 716 (2014).
21. U.R. Ghodake, N.D. Chaudhari, R.C. Kambale, J.Y. Patil, and S.S. Suryavanshi, *J. Magn. Magn. Mater.* 407, 60 (2016).
22. J. Smit, *Magnetic Properties of Materials* (New York: McGraw-Hill Book Co., 1971), p. 216.
23. C. Sujatha, K. Venugopal Reddy, K. Sowri Babu, A. RamaChandra Reddy, and K.H. Rao, *Phys. B* 407, 1232 (2012).
24. J. Smit and H.P.J. Wijn, *Ferrites* (Eindhovan: Philips Technical Library, 1959), p. 149.
25. S.E. Shirsath, S.M. Patange, R.H. Kadam, M.L. Mane, and K.M. Jadhav, *J. Mol. Struct.* 1024, 77 (2012).
26. M.A. Ahmed, E. Ateia, L.M. Salah, and A.A. El-Garnal, *Mater. Chem. Phys.* 92, 310 (2005).
27. M. Azhar Khan, M.U. Islam, M. Ishaque, and I.Z. Rahman, *Ceram. Int.* 37, 2519 (2011).
28. A. Globus, H. Pascard, and V.J. Cagan, *J. Dephys. Colloque.* C1, 163 (1997).
29. M.A. Hakim, S.K. Nath, S.S. Skider, and K.H. Maria, *J. Phys. Chem. Solids* 74, 1316 (2013).
30. M.A. Amer and O.M. Hemeda, *Hyperfine Interact.* 96, 99 (1995).
31. R.D. Waldron, *Phys. Rev.* 99, 1727 (1955).
32. K.B. Modi, S.J. Shah, N.B. Pujara, T.K. Pathak, N.H. Vasoya, and I.J. Jhala, *J. Mol. Struct.* 1049, 250 (2013).
33. B.K. Labde, M.C. Sable, and N.R. Shamkuwae, *Mater. Lett.* 57, 1651 (2003).
34. S.A. Patil, V.C. Mahajan, A.K. Ghatage, and S.D. Lotke, *Mater. Chem. Phys.* 57, 86 (1998).
35. C. Kittel, *Introduction to Solid State Physics,* 5th ed. (New York: John Wiley and Sons, Inc., 1976).
36. B. Johnson and A.K. Walton, *Br. J. Appl. Phys.* 16, 475 (1965).
37. W.D. Callister, *Materials Science and Engineering, An Introduction*, 4th ed. (NewYork: Wiley, 2000), p. 714.
38. A. Kumar, *Introduction to Solid State Physics* (New Delhi: PHI Learning Private Ltd., 2010), p. 76.
39. E.J.W. Verwey and E.L. Heilmann, *J. Chem. Phys.* 15, 174 (1947).
40. M.S. Khandekar, R.C. Kamble, J.Y. Patil, Y.D. Kolekar, and S.S. Suryavanshi, *J. Alloys Compd.* 509, 1861 (2011).
41. K.W. Wagner, *Am. Phys.* 40, 817 (1913).
42. M. Penchal Reddy, H. Gon Kim, D.S. Yoo, W. Madhuri, N.R. Reddy, K.V. Siva Kumar, and R.R. Reddy, *Mater. Sci. Appl.* 3, 628 (2012).
43. C.G. Koops, *Phys. Rev.* 83, 121 (1951).
44. D.A. Adler and J. Feinleib, *Phys. Rev. B* 2, 3112 (1970).
45. S.S. Khot, N.S. Shinde, B.P. Ladgaonkar, B.B. Kale, and S.C. Watawe, *Adv. Appl. Sci. Res.* 2, 460 (2011).
46. A. Globus, P. Duplex, and M. Guyot, *IEEE Trans.* 7, 617 (1971).
47. B.P. Jacob, S. Thankachan, S. Xavier, and E.M. Mohammed, *J. Alloys Compd.* 541, 29 (2012).